

# Supplement to “Catching Shaped Microwave Photons with 99.4% Absorption Efficiency”

J. Wenner<sup>1</sup>, Yi Yin<sup>1,2</sup>, Yu Chen<sup>1</sup>, R. Barends<sup>1</sup>, B. Chiaro<sup>1</sup>, E. Jeffrey<sup>1</sup>, J. Kelly<sup>1</sup>, A. Megrant<sup>1,3</sup>, J. Mutus<sup>1</sup>, C. Neill<sup>1</sup>, P. J. J. O’Malley<sup>1</sup>, P. Roushan<sup>1</sup>, D. Sank<sup>1</sup>, A. Vainsencher<sup>1</sup>, T. C. White<sup>1</sup>, Alexander N. Korotkov<sup>4</sup>, A. N. Cleland<sup>1</sup>, and John M. Martinis<sup>1</sup>  
<sup>1</sup>*Department of Physics, University of California, Santa Barbara, California 93106, USA*  
<sup>2</sup>*Department of Physics, Zhejiang University, Hangzhou 310027, China*  
<sup>3</sup>*Department of Materials, University of California, Santa Barbara, California 93106, USA and*  
<sup>4</sup>*Department of Electrical Engineering, University of California, Riverside, California 92521, USA*

## THEORETICAL CAPTURE EFFICIENCIES

Here, we calculate the reflected signal and receiver efficiency for tunably-coupled resonator driven with several different drive pulse shapes. For a time constants near  $2/\kappa$ , exponentially increasing drive pulses are more efficient than rectangular and exponentially decreasing pulses. We then show that optimal efficiencies require that the resonator have zero intrinsic loss and be driven at the resonance frequency.

### Transmission Coefficients

Consider a resonator driven through a tunable coupler with transmission and reflection coefficients defined in Fig. S1. These coefficients are related by [1]

$$\mathbf{t}_1 = \frac{R_2}{R_1} \mathbf{t}_2, |\mathbf{t}_1|^2 \frac{R_1}{R_2} + |\mathbf{r}|^2 = 1, \mathbf{r}_2 = -\mathbf{r}_1^* \frac{\mathbf{t}_1}{\mathbf{t}_1^*}, \quad (\text{S1})$$

where  $R_1 \simeq 50 \Omega$  ( $R_2$ ) is the drive (resonator) impedance,  $\mathbf{t}_1$  ( $\mathbf{t}_2$ ) is the transmission coefficient into (from) the resonator, and  $\mathbf{r}_1$  ( $\mathbf{r}_2$ ) is the reflection coefficient on the drive (resonator) side, where  $|\mathbf{r}_1| = |\mathbf{r}_2| = |\mathbf{r}|$ .

The transmission coefficients are related to the coupling quality factor  $Q_c$  by

$$Q_c = \frac{\omega \tau_{rt} R_1}{|\mathbf{t}_2|^2 R_2},$$

where  $\tau_{rt}$  is the ratio of the resonator energy to the travelling wave power and  $\omega/2\pi = 6.55 \text{ GHz}$  is the resonator frequency. For a  $\lambda/4$  coplanar waveguide resonator [1],

$$\tau_{rt} \approx \pi/\omega. \quad (\text{S2})$$

With our device,  $\kappa \tau_{rt} \ll 1$  as the coupler energy decay rate  $\kappa$  is within the range  $[1/(3 \mu\text{s}), 1/(50 \text{ ns})]$ . According to [2],  $\kappa$  is given by  $Q_c = \omega/\kappa$ , so

$$\frac{|\mathbf{t}_1|^2}{\tau_{rt}} = \kappa \frac{R_2}{R_1}. \quad (\text{S3})$$

Note that  $|\mathbf{t}_1|^2 \ll 1$  as the coupler is near the grounded end of the resonator.

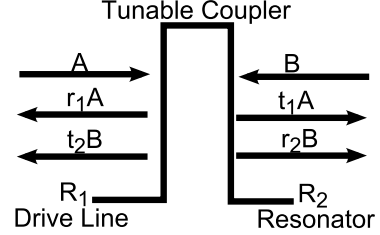


FIG. S1: Transmission and reflection coefficient notation. An  $R_1 \simeq 50 \Omega$  drive transmission line is coupled to an  $R_2 \simeq 80 \Omega$  resonator via a tunable coupler (barrier).  $A$  is the incoming signal from the drive line, whereas  $B$  is the signal reaching the coupler from the resonator. The coupler has reflection coefficient  $\mathbf{r}_1$  on the drive side, reflection coefficient  $\mathbf{r}_2$  on the resonator side, transmission coefficient from the drive line  $\mathbf{t}_1$ , and transmission coefficient from the resonator  $\mathbf{t}_2$ .

### Absorption Efficiencies

Suppose that two signals reach the coupler at time  $t$ : an incoming drive  $A(t)$  and a signal  $B(t)$  from the resonator (see Fig. S1). Then,  $B(t)$  is described by [1]

$$\dot{B} = \frac{\mathbf{r}_2 e^{i\phi} - 1}{\tau_{rt}} B + \frac{\mathbf{t}_1 e^{i\phi}}{\tau_{rt}} A - \frac{1}{2T_1} B, \quad (\text{S4})$$

where  $T_1$  is the intrinsic resonator energy decay time and  $\phi = \tau_{rt} \delta\omega - \arg(\mathbf{r}_2)$  arises from a detuning  $\delta\omega$  between the drive and resonator frequencies. Note that

$$e^{i\phi} = \frac{\mathbf{r}_2^*}{|\mathbf{r}|} e^{i\tau_{rt} \delta\omega},$$

so Eq. (S4) simplifies to

$$\dot{B} = \left( -\frac{\kappa}{2} B + \frac{\mathbf{t}_1 \mathbf{r}_2^*}{\tau_{rt} |\mathbf{r}|} A \right) - \frac{1}{2T_1} B + \delta\omega \left( iB + \mathbf{t}_1 \frac{\mathbf{r}_2^*}{|\mathbf{r}|} A \right) \quad (\text{S5})$$

with Eq. (S3) and  $\kappa \tau_{rt}, \tau_{rt} \delta\omega, |\mathbf{t}_1|^2 \ll 1$ . Here, the time-dependence is contained in  $A$ ,  $B$ , and potentially  $x$ .

We initially consider a simple case where the coupling is time-independent, the drive is on resonance, and the resonator intrinsic quality factor is infinite. In this case,

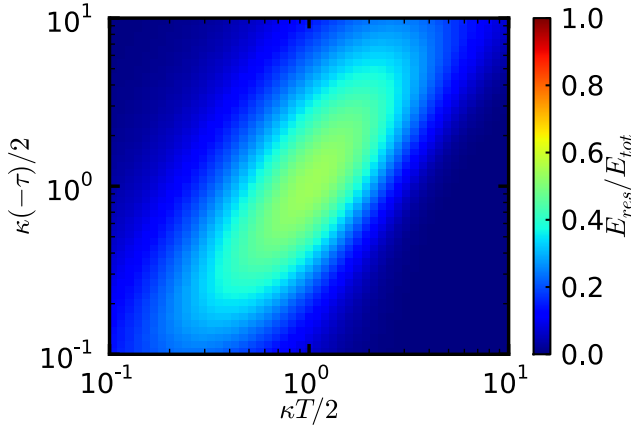


FIG. S2: Receiver efficiency for infinite exponentially decreasing drive. If the drive is infinitely long ( $T' \rightarrow \infty$ ) but the coupler closes at  $T$ , the receiver efficiency is maximized when  $-\tau = T = 2/\kappa$  and is then 54.1%.

solving for  $B(t)$  gives

$$B(t) = B(0)e^{-\kappa t/2} + e^{-\kappa t/2} \frac{\mathbf{t}_1 \cdot \mathbf{r}_2^*}{\tau_{rt} |\mathbf{r}|} \int_0^t A(t') e^{\kappa t'/2} dt'. \quad (\text{S6})$$

The power in the resonator is  $|B(t)|^2/2R_2$ . The energy  $E_{res}$  in the resonator is thus  $|B(t)|^2 \tau_{rt}/2R_2$  from the definition of  $\tau_{rt}$ . If the resonator is initially unpopulated,

$$E_{res} = \frac{1}{2R_1} \kappa e^{-\kappa T} \left| \int_0^T A(t) e^{\kappa t/2} dt \right|^2 \quad (\text{S7})$$

after a time  $T$ . The total energy  $E_{tot}$  equals the integral

$$E_{tot} = \frac{1}{2R_1} \int_0^{T'} |A(t)|^2 dt \quad (\text{S8})$$

of the drive power  $|A(t)|^2/2R_1$  applied for  $t \in (0, T')$ . The ratio  $E_{res}/E_{tot}$  is defined to be the receiver efficiency; note the factors  $1/2R_1$  cancel.

### Rectangular Pulses

Suppose the resonator is driven by a rectangular pulse,  $A(t) = A_0$  for  $0 \leq t \leq T = T'$ . Then, the receiver efficiency is

$$\frac{E_{res}}{E_{tot}} = \frac{4}{\kappa T} \left(1 - e^{-\kappa T/2}\right)^2, \quad (\text{S9})$$

which is plotted in Fig. 4(a) of the main text. This efficiency reaches a maximal value of 81.4529% when  $T = 2.51286/\kappa$ .

### Exponential Pulses

Suppose that the resonator is driven by an exponential pulse,  $A(t) = A_0 e^{t/\tau}$  for  $0 \leq t \leq T'$  and the coupler

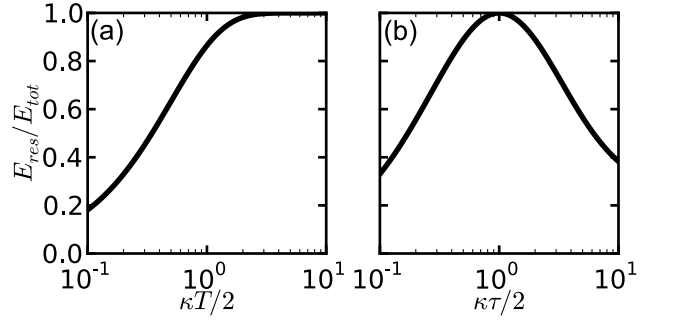


FIG. S3: Receiver efficiency for exponentially increasing drive. The efficiency is shown versus (a) pulse length  $T$  ( $\tau = 2/\kappa$ ) and (b) time constant  $\tau$  ( $T \rightarrow \infty$ ). The efficiency is maximized for  $\tau = 2/\kappa$ ,  $T \rightarrow \infty$ . The regime for efficiencies  $> 90\%$  is shown in Fig. 3(a),(b) of the main text.

closed at  $t = T$ . Then, the receiver efficiency is

$$\frac{E_{res}}{E_{tot}} = \frac{4 \left(\frac{2}{\kappa\tau}\right) (e^{T/\tau} - e^{-\kappa T/2})^2}{\left(1 + \frac{2}{\kappa\tau}\right)^2 (e^{2T'/\tau} - 1)}. \quad (\text{S10})$$

This is true for both exponentially decreasing ( $\tau < 0$ ) and exponentially increasing ( $\tau > 0$ ) pulses.

The case  $\tau < 0$ ,  $T' \rightarrow \infty$  corresponds to a source excitation which naturally decays via static coupling. Here, the receiver efficiency reduces to

$$\frac{E_{res}}{E_{tot}} = \frac{4 \left(\frac{2}{\kappa(-\tau)}\right) (e^{-T/(-\tau)} - e^{-\kappa T/2})^2}{\left(1 - \frac{2}{\kappa(-\tau)}\right)^2} \quad (\text{S11})$$

and is plotted in Fig. S2. It is maximized when  $-\tau = T = 2/\kappa$  with an efficiency of  $4/e^2 = 54.134\%$ .

For the  $\tau < 0$ ,  $T' = T$  case, a truncated natural drive, the efficiency is plotted in Fig. 4(b) of the main text. The efficiency is continuous even at  $\tau = -2/\kappa$  where

$$2R_1 E_{res} = A_0^2 T^2 \kappa e^{-\kappa T}.$$

For a constant pulse length, the efficiency is maximized in the limit  $\tau \rightarrow -\infty$ . This limit corresponds to a rectangular pulse, and  $E_{res}/E_{tot}$  reduces to the rectangular value. For a constant time constant, the efficiency is maximized at pulse lengths which increase asymptotically as  $\tau \rightarrow -\infty$  to the rectangular maximum of  $2.51286/\kappa$ . In addition, the efficiency always approaches zero for infinite pulse lengths as the excitation has infinite time to decay.

An exponentially increasing ( $\tau > 0$ ,  $T' = T$ ) drive pulse is ideal for static coupling; the receiver efficiency Eq. (S10) is plotted in Fig. 4(d) of the main text. As predicted [1], the efficiency for constant pulse lengths is maximized when  $\tau = 2/\kappa$ , where it reduces to  $1 - e^{-\kappa T}$  and so asymptotically approaches unity as  $T \rightarrow \infty$  (see Fig. S3(a)). For a fixed time constant, the efficiency is

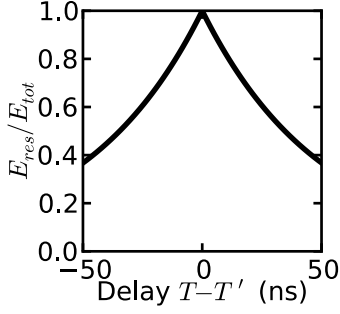


FIG. S4: Receiver efficiency versus offset between closing coupler ( $T$ ) and stopping drive ( $T'$ ). The efficiency is shown for an exponentially increasing pulse with  $\tau = 2/\kappa$ ,  $T = 8/\kappa$ ,  $\kappa = 1/(50 \text{ ns})$ . The regime for efficiencies  $> 90\%$  is shown in Fig. 3(d) of the main text. The exponential decay for  $T < T'$  is due to the particular drive pulse shape, while that for  $T' < T$  is universal.

maximized at  $T \rightarrow \infty$  for  $\tau \leq 2/\kappa$  and at lengths asymptotically approaching the rectangular limit as  $\tau \rightarrow \infty$ . At such pulse lengths, the efficiency is greater than rectangular limit of  $81.5\%$  for  $\tau > 0.8/\kappa$ . For infinite duration pulses, the efficiency simplifies to

$$\frac{E_{res}}{E_{tot}} = \frac{4 \left( \frac{\kappa\tau}{2} \right)}{\left( 1 + \frac{\kappa\tau}{2} \right)^2},$$

which is greater than  $81.5\%$  for  $0.8 < \kappa\tau < 5$ , as shown in Fig. S3(b).

### Coupler Closing Delay

Now suppose that the coupler is closed and the drive stopped at slightly different times  $T$  and  $T'$ , respectively. If the drive is stopped first ( $T' < T$ ), the receiver efficiency is decreased by a factor of  $e^{-\kappa(T-T')}$  according to Eq. (S6), regardless of the pulse shape. If the coupler is closed first ( $T < T'$ ), the receiver efficiency is changed by a factor which depends on the particular drive pulse. For an exponential pulse, the receiver efficiency is reduced by a factor of

$$\left( \frac{e^{T/\tau} - e^{-\kappa T/2}}{e^{T'/\tau} - e^{-\kappa T'/2}} \right)^2,$$

as shown in Fig. S4.

### Reflections - Destructive Interference

The basis for these high absorption efficiencies is destructive interference between the reflection  $\mathbf{r}_1 A$  and re-emission  $\mathbf{t}_2 B$  signals. This requires opposite phases for these signals. Since the phase of  $A$  adds to the phase of  $B$ , we assume without loss of generality that  $A$  is positive. The phase of the reflection signal is then given by

$\mathbf{r}_1$ , which by Eq. (S1) is the phase of  $-\mathbf{r}_2^* \mathbf{t}_1^2$ . The phase of the re-emission signal is given by the phase of  $\mathbf{t}_2$ , which by Eq. (S1) is the phase of  $\mathbf{t}_1$ , and the phase of  $B$ , which by Eq. (S6) is the phase of  $\mathbf{t}_1 \mathbf{r}_2^*$ . Thus, the reflection and re-emission signals are always opposite in phase (see Fig. S8).

### Drive Frequency

We now start to consider the effects of relaxing our simplifying assumptions. First, we detune the drive frequency by a small  $\delta\omega$  from the resonator frequency  $\omega$  while we still assume that the resonator is lossless and the coupling is static. The capture efficiencies can then be solved with Eq. (S5). The resonator frequency is included here not only in  $\delta\omega$  but also  $\tau_{rt}$  according to Eq. (S2).

For the exponentially increasing pulse, a nonzero detuning reduces the maximum receiver efficiency. As the detuning increases, not only is the maximum receiver efficiency reduced but the values of  $\tau$  and  $T$  which maximize the efficiency are reduced as shown in Fig. S5(a)-(c). For the ratio of the efficiency to the efficiency with  $\delta\omega = 0$ , the frequency width of the peak is independent of  $T$  for  $\tau = 2/\kappa$  and  $T \geq 3/\kappa$  [Fig. S5(d)] but is proportional to the coupling  $\kappa$  [Fig. S5(e)]. In addition, the receiver efficiency is maximized in the case of  $\delta\omega = 0$ .

We have also verified numerically that the receiver efficiency is maximized when  $\delta\omega = 0$  for rectangular, exponentially increasing, and exponentially decreasing drive pulses, even when the pulse lengths and time constants are varied. The efficiency is also an even function of the detuning. In addition, this is even true when the intrinsic resonator loss is nonzero.

### Intrinsic Loss

Suppose the resonator has intrinsic loss characterized by a decay time  $T_1$  but the detuning is zero and the coupling is static. Then, Eq. (S5) reduces to

$$\dot{B} = \left( -\frac{\kappa}{2} - \frac{1}{2T_1} \right) B + \frac{\mathbf{t}_1 \mathbf{r}_2^*}{\tau_{rt} |\mathbf{r}|} A,$$

where the receiver efficiency can be found as before. Now suppose that the time-dependence of  $A(t)$  can be expressed as a function of  $t/\tau$  for some time constant  $\tau$ ; this is valid for both rectangular and exponential pulses. Then, this efficiency incorporating  $T_1$  equals that calculated from Eqs. (S7)-(S8) with the following modifications:

1.  $T' \rightarrow \frac{\kappa+1/T_1}{\kappa} T'$
2.  $T \rightarrow \frac{\kappa+1/T_1}{\kappa} T$
3.  $\tau \rightarrow \frac{\kappa+1/T_1}{\kappa} \tau$

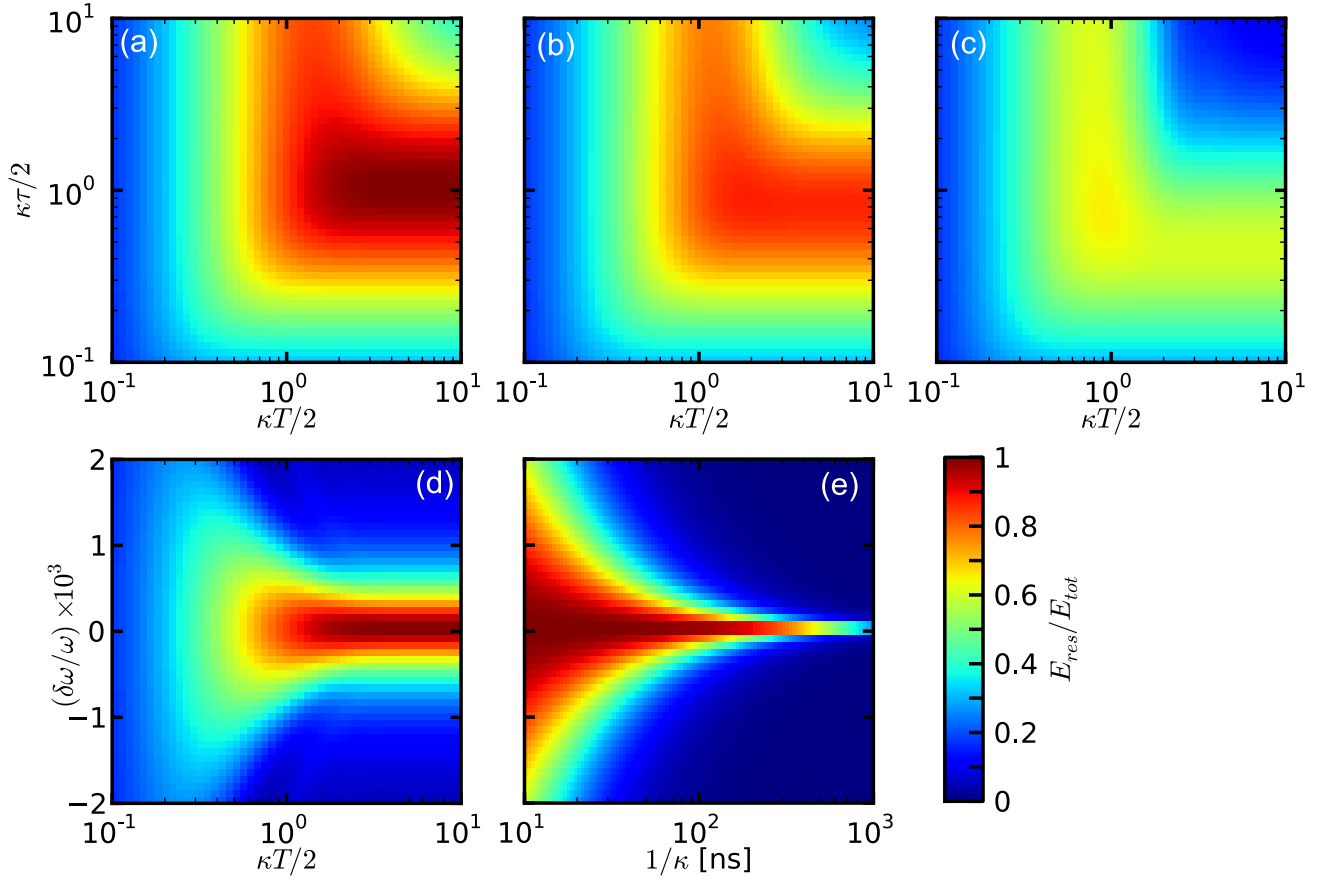


FIG. S5: Effect of detuned drive frequency on receiver efficiency. Unless otherwise stated, theory is for the experimental system with frequency  $\omega/2\pi = 6.55$  GHz, coupling  $\kappa = 1/(50 \text{ ns})$ , pulse length  $T = 8/\kappa$ , and exponential time constant  $\tau = 2/\kappa$ . (a)-(c) The receiver efficiency is plotted vs  $T$  and  $\tau$  for three fractional detunings  $\delta\omega/\omega$ : (a) 0, (b) 0.0002 [1.3 MHz], and (c) 0.0005 [3.3 MHz]. (d) The receiver efficiency is plotted vs  $T$  and  $\delta\omega/\omega$ . The efficiency is maximized when the drive and resonator frequencies are equal with the frequency width effectively independent of  $T$  for  $\kappa T > 3$ . (e) The receiver efficiency is plotted vs  $1/\kappa$  and  $\delta\omega/\omega$  for fixed  $\kappa T$ ,  $\kappa\tau$ . The frequency width is proportional to  $\kappa$ .

4. The receiver efficiencies are reduced by  $\frac{\kappa}{\kappa + \frac{1}{T_1}}$ .

For example, the receiver efficiency for an exponential pulse is

$$\frac{E_{res}}{E_{tot}} = \frac{4 \left( \frac{2}{(\kappa + \frac{1}{T_1})\tau} \right) \left( e^{T/\tau} - e^{-(\kappa + \frac{1}{T_1})T/2} \right)^2}{\left( 1 + \frac{2}{(\kappa + \frac{1}{T_1})\tau} \right)^2 (e^{2T/\tau} - 1)} \frac{\kappa}{\kappa + \frac{1}{T_1}},$$

which is just Eq. (S10) with these modifications. Note that  $(\kappa + \frac{1}{T_1})$  is just the measured decay constant when performing a typical  $T_1$  measurement with a given  $\kappa$ .

## EXPERIMENTAL METHODS

Here we describe our experimental setup along with how we extract absorption efficiencies from the raw data. We then describe how to use the superconducting phase qubit to experimentally calibrate the couplings between the resonator and the transmission line, delay times between the various control lines, and the resonator drive energy. We demonstrate the independence of the absorption efficiency on the drive power and number of averages.

### Experimental Setup and Measurement

The device is the same as was used in Ref. [3], as shown in Fig. S6. This multi-layer device was patterned using standard photolithography [4]. All metal films were sputter-deposited Al, with *in situ* Ar ion milling prior to deposition; they were etched with a  $\text{BCl}_3/\text{Cl}_2$  inductively-coupled plasma [5]. The phase qubit and SQUID (superconducting quantum interference device) are comprised of Al/ $\text{AlO}_x$ /Al junctions. The phase qubit capacitor and crossovers were created using a hydro-genated amorphous silicon dielectric.

The chip with the resonator is mounted on the 30 mK stage of a dilution refrigerator. The chip is located in an Al sample mount [6] placed in a high-permeability magnetic shield. This protects against magnetic vortex losses and prevents magnetic fields from other components, such as circulators and switches, from changing the device calibration.

We generate the resonator drive pulse with a digital-to-analog converter (DAC) [3, 4, 7, 8]. Each board contains two channels with a one-gigasample-per-second 14-bit DAC chip; the outputs correspond to the  $I$  (cosine) and  $Q$  (sine) quadratures. Both outputs are mixed by an  $IQ$ -mixer with a continuous  $\sim 6.4$  GHz sine wave from a local oscillator (LO), as shown in the schematic of Fig. S7. The LO is detuned by  $f_{sb} = 165$  MHz from the resonator frequency to prevent spurious residual signal at the LO frequency from exciting the resonator; we compensate for this with the  $I$  and  $Q$  signals. We calibrate out mixer imperfections as explained in [8].

To reach the single-photon level, we attenuate the drive signal and amplify the reflected signal, as shown in Fig. S7. In particular, we attenuate thermal noise with 20 dB of attenuation at 4 K and 40 dB of attenuation at 30 mK. We separate out the reflections on the drive line with a circulator. The reflections then pass through two circulators to isolate the resonator from thermal noise and are then amplified by  $\sim 35$  dB at 4 K with a low noise HEMT (high-electron mobility transistor) amplifier; there is additional amplification at room temperature.

We measure the amplified reflection signal with a room temperature analog-to-digital converter (ADC) [3, 7]. We

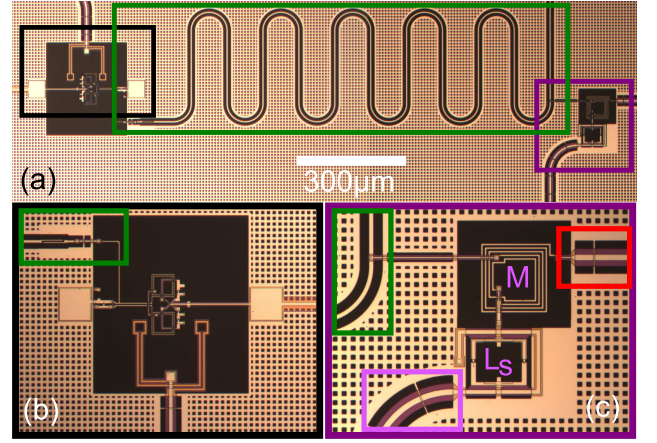


FIG. S6: Photomicrograph of experimental device, showing chip (a), superconducting phase qubit (b), and tunable coupler (c). Qubit, resonator, coupler, coupler bias line, and drive/measure line are respectively in black, green, dark purple, light purple, and red. Qubit is used for calibrating coupler.

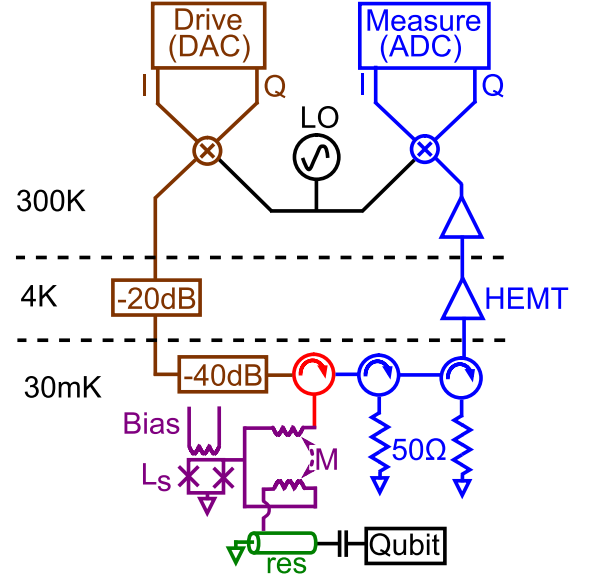


FIG. S7: Experimental schematic. The resonator is driven through a tunable coupler (consisting of a mutual inductance  $M$  modulated by a SQUID with inductance  $L_s$ ). The drive signal is generated by a digital-to-analog converter (DAC), mixed with local oscillator (LO) at 6.4 GHz, and attenuated. Signals reflected from the coupler and leaking from the resonator are separated from the drive path using a circulator. These output signals then pass through two circulators for thermal noise isolation, are amplified at 4 K by a HEMT amplifier and then further at room temperature, are heterodyne mixed with an  $IQ$  mixer using the drive LO, and then are measured using an analog-to-digital converter (ADC).

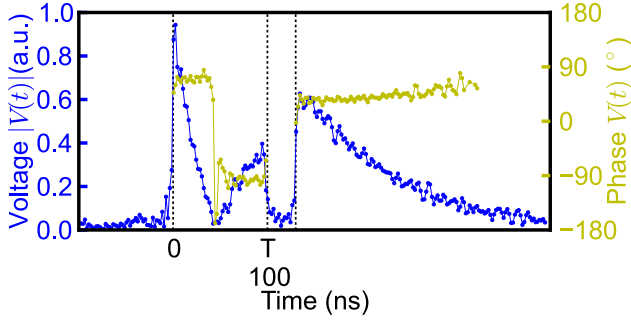


FIG. S8: Measured output phase. The resonator is driven with an exponentially decreasing drive pulse from  $t = 0$  to  $T = 100$  ns; the coupler is closed for 30 ns and reopened (same as Fig. 2(a) of main text). The output voltage is shown versus time in both magnitude (blue) and phase (yellow for  $|V(t)| \neq 0$ ). The magnitude goes to zero when the phase changes by  $\pi$ , so dominant loss source shifts from reflection to reemission.

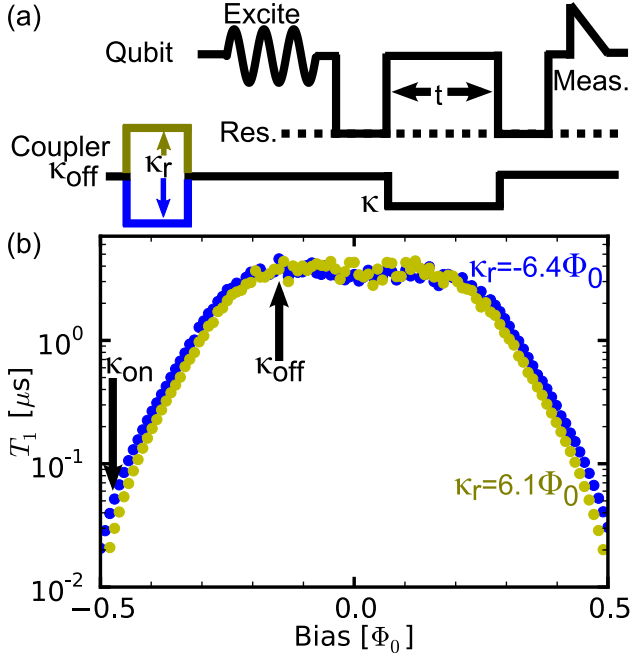


FIG. S9: Calibrating coupling. (a) Pulse sequence. We first reset the coupler while resetting the qubit into the ground state. We then excite the qubit and swap the excitation into the resonator. After a time  $t$  with the excitation in the resonator, any remaining excitation is swapped back into the qubit and then measured. (b) The decay time  $T_1$  is plotted versus the coupler bias current, expressed as a flux  $\Phi$  through the SQUID divided by the flux quantum  $\Phi_0 = h/2e$ . Decay times are shown for two coupler reset biases,  $+6.1\Phi_0$  (yellow) and  $-6.4\Phi_0$  (blue). With the  $-6.1\Phi_0$  bias, we define the coupling  $\kappa_{\text{on}}$  to be on when  $T_1 = 1/50$  ns; this is where we drive the resonator and allow reemission. When  $T_1$  is maximized, the coupling  $\kappa_{\text{off}}$  is zero and so is turned off.

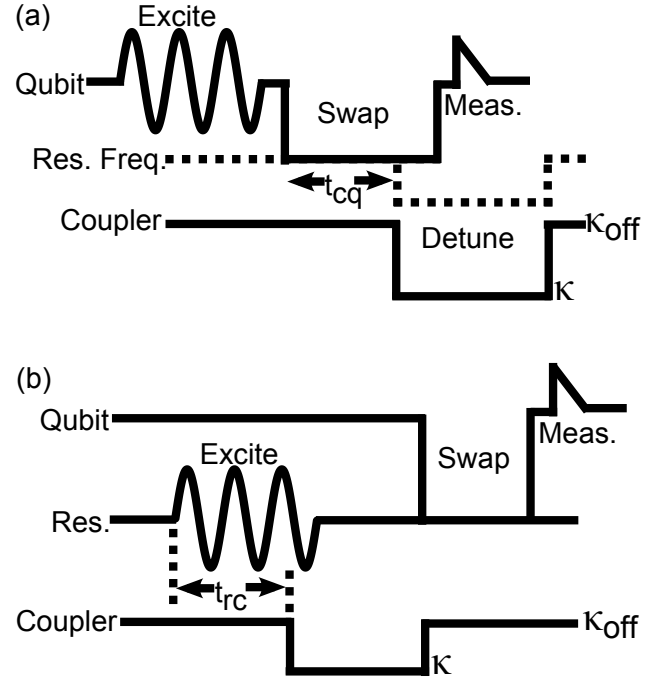


FIG. S10: Correcting for inter-line delays. (a) To measure the coupler-qubit delay  $t_{cq}$ , we excite the qubit, swap the excitation into the resonator detuned by opening the coupler, and measure the qubit. (b) To measure the resonator-coupler delay  $t_{rc}$ , we drive the resonator and open the coupler for the same duration but offset by  $t_{rc}$ . We then swap any resonator excitation to the qubit, which is then measured.

first down-convert the signal with an  $IQ$ -mixer using the LO signal. The resulting  $I$  and  $Q$  quadrature voltages are then measured versus time using two 500-megasample-per-second 8-bit ADC chips and are then averaged  $\sim 3,000,000$  times.

We then filter the raw  $V(t) = I + iQ$  data. We first rescale the  $Q$  data by an experimentally measured factor to accommodate differences in electronics between the two quadratures. We then subtract the average value of  $V(t)$  as measured prior to the drive to remove DC components. We then multiply by  $e^{i2\pi f_{sb} t}$  to determine the signal at the drive frequency. To remove crosstalk signals, we digitally apply a sharp low-pass filter at 150 MHz.

After this filtering, we notice that the phase of  $V(t)$  changes by  $\pi$  when the magnitude drops to near-zero (Fig. S8). This indicates a shift from  $V(t)$  dominated by retransmission before this time to reemission afterwards and also demonstrates that retransmission and reemission destructively interfere.

In calculating the energy  $\int |V(t)|^2 dt$  in each portion of the pulse sequence, any noise appears to be additional energy. To subtract out this spurious contribution, our procedure (as rigorously derived in the “Error Analysis” section) involves:

- Calculate the energy prior to driving the resonator,



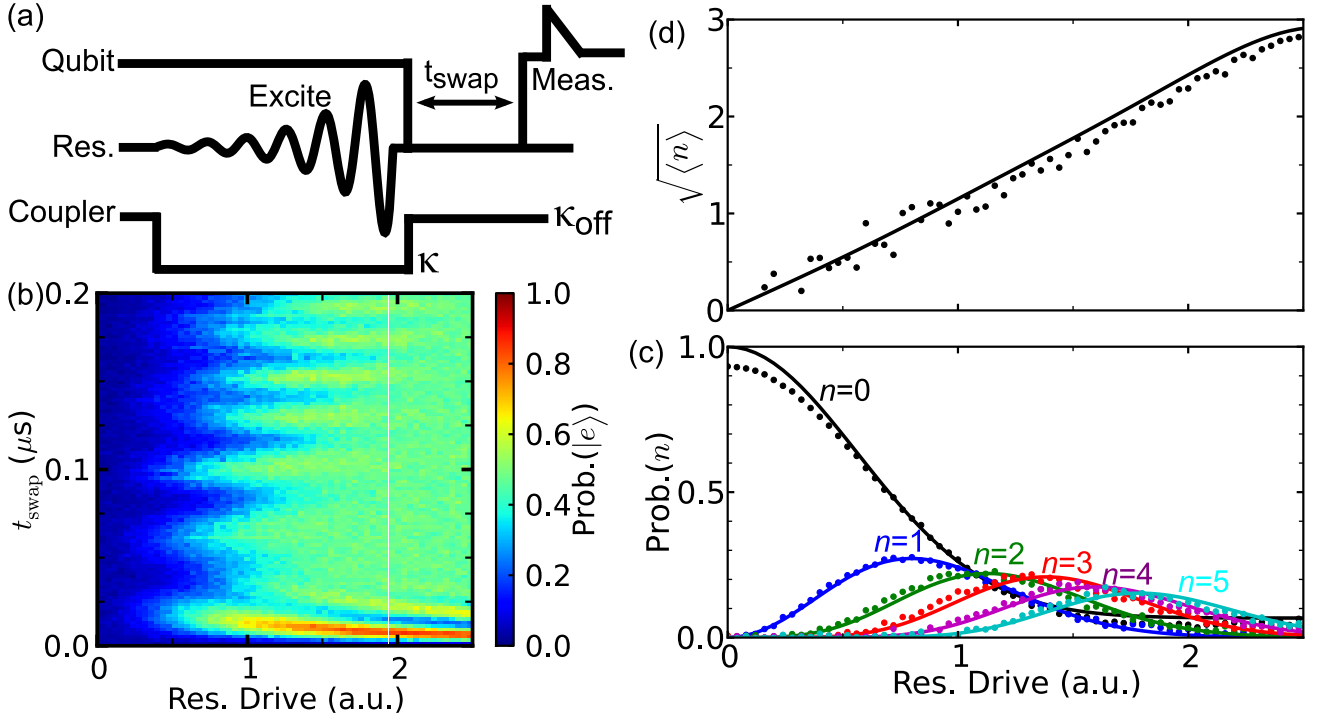


FIG. S11: Calibrating drive energy. (a) With the coupler open, we drive the resonator with various drive amplitudes. We then swap any excitation to the qubit for varying times  $t_{\text{swap}}$  and measure the qubit. (b) The qubit excited state ( $|e\rangle$ ) probability is shown versus the drive amplitude and  $t_{\text{swap}}$ . For these pulses, we used a  $1\ \mu\text{s}$  exponentially increasing pulse with  $\tau = 2/\kappa$ . (c) Probability for the resonator to be in the  $n$ th Fock state, fit to the data in (b), versus drive amplitude. States with  $n > 5$  are not shown. (d) The average photon number from the probabilities in (c) is shown versus resonator drive amplitude.

where there is no signal

- Rescale the noise energy to determine the noise energy in the desired integration region
- Subtract this noise energy from the total measured energy in a desired region.

### Calibrating Coupling & Delays

The tunable coupler employs a tunable mutual inductance between the drive and resonator [3]. The mutual inductance  $M$  consists of two interwound coils which are galvanically connected, as shown in Fig. S6(c) and Fig. S7. From this connection, a SQUID (superconducting quantum interference device) is attached with tuning inductance  $L_s$ . This tuning arises from a flux induced by an on-chip coupler bias current which is externally generated.

We calibrate the coupling  $\kappa \propto (M - L_s)^2$  [3] in terms of this current with a superconducting phase qubit capacitively coupled to the resonator [3, 9, 10]. Using the qubit, we generate a single photon and swap it to the resonator [Fig. S9(a)]. We then apply the desired coupler bias for varying times, after which we swap to the qubit and measure the residual excitation. From the decay of

the excitation probability  $P_e$ , we extract the resonator decay time  $T_1$ , shown in Fig. S9(b). At the bias maximizing  $T_1$ , the coupling is zero and hence closed, as verified by trying to drive the resonator; here,  $T_1$  is the intrinsic resonator decay time  $1/\kappa_i \simeq 3\ \mu\text{s}$  since  $1/T_1 = \kappa + \kappa_i$ . We define the coupler to be open and drive the resonator when  $T_1 \simeq 50\ \text{ns}$ .

However, the open coupling can range from  $1/(50\ \text{ns})$  to  $1/(30\ \text{ns})$ , since the SQUID has multiple potential wells, each with a different coupling (see Fig. S9(b)). We reproducibly select a particular well by adding a coupler reset pulse prior to all pulse sequences.

Adjusting the SQUID to tune the coupler modulates the resonator inductance to ground [3]. This adjusts the resonator frequency by  $\sim 20\ \text{MHz}$  between the opened and closed biases. Hence, opening the coupler to detune the resonator blocks swaps between the qubit and resonator as tuned with the coupler closed.

We use this to tune the temporal delay  $t_{cq}$  between the qubit and coupler [Fig. S10(a)]. We first excite the qubit, swap the excitation to the resonator while opening the coupler, and measure the qubit. As we vary  $t_{cq}$ , the time for which the qubit excited state probability  $P_e$  is maximized is the actual delay.

To calibrate the delay  $t_{rc}$  between the resonator drive and the coupler, we employ the sequence in Fig. S10(b).

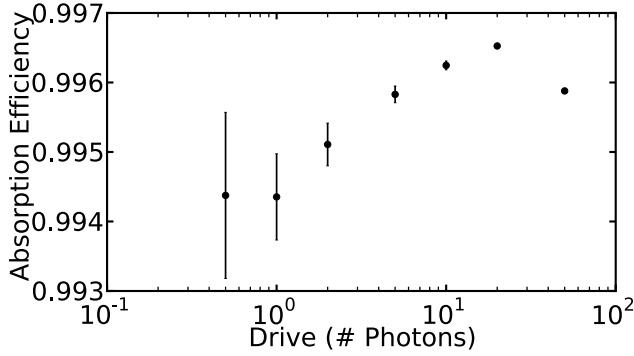


FIG. S12: Drive energy independence of absorption efficiency. The absorption efficiency is independent of the resonator drive energy for energies of 0.5-50 photons. Data are shown for exponentially increasing drive pulses with time constant  $\tau = 2/\kappa$  and length  $20/\kappa$ , and error bars indicate statistical errors from Eq. (S16).

Here, we drive the resonator with a many-photon pulse to ensure resonator excitation. For this time but offset by  $t_{rc}$ , we open the coupler. Any induced resonator excitation is then swapped into the qubit and measured. Hence, the actual delay is when  $P_e$  is maximized. As explained in the main text, we verify this timing by varying when the coupler is closed relative to stopping the drive and maximizing the absorption efficiency.

### Drive Energy

We use the qubit to calibrate the resonator drive energy in terms of the drive amplitude [3, 11]. We vary the drive amplitude for a particular drive pulse shape. For each amplitude, we drive the resonator, swap between the qubit and resonator for varying swap times  $t_{\text{swap}}$ , and measure the qubit excited state probability  $P_e$  [Fig. S11(a),(b)]. We simulate this probability versus  $t_{\text{swap}}$  using the Linblad master equation for  $n$ -photon Fock states. We least-squares fit the experimental and theoretical probabilities to determine for each drive amplitude the experimental Fock state distribution, shown in Fig. S11(c). We fit this measured distribution to a Poisson distribution,

$$P_n^{\text{Poisson}} = \frac{\langle n \rangle^n e^{-\langle n \rangle}}{n!},$$

as the resonator is in a classically-driven coherent state. From this fit, we extract the mean number of photons  $\langle n \rangle$  captured in the resonator [Fig. S11(d)] and find a linear fit between drive amplitude and  $\sqrt{\langle n \rangle}$ . We then rescale this according to the measured absorption efficiency to determine the drive amplitude necessary for a single photon drive ( $\langle n \rangle = 1$ ).

To determine if the exact calibration matters, we measured the absorption efficiency versus resonator drive am-

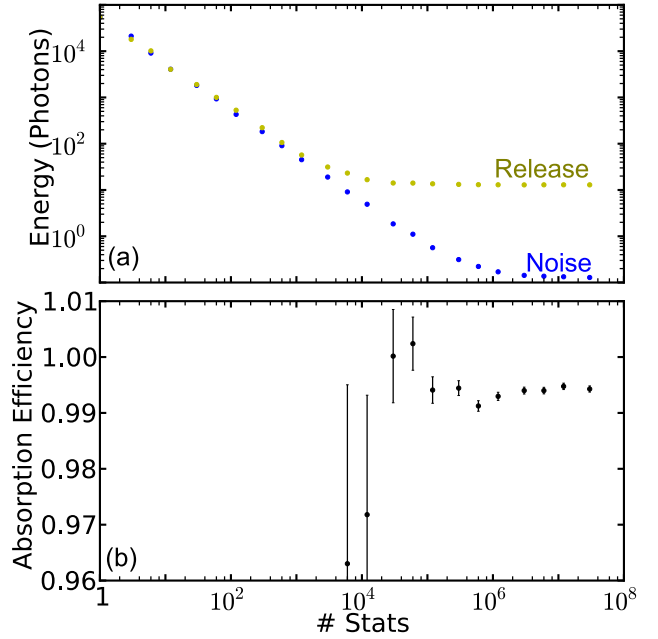


FIG. S13: Varying number of averages. (a) The noise (blue) and release signal (yellow) energies are shown for varying numbers of averages. The noise energy has been rescaled by the duration of the energy release phase of the pulse sequence (See Fig. 2 of the main text). These are measured for exponentially increasing drive pulses with time constant  $\tau = 2/\kappa$  and length  $20/\kappa$ . The release energy flattens out where it no longer equals the noise energy. (b) Absorption efficiencies versus number of averages. Data are only shown where the noise energy is substantially less than the release energy so that absorption efficiencies make sense. Error bars indicate statistical errors from Eq. (S16) and are approximately 6% the noise-to-signal ratio.

plitude. As shown in Fig. S12, the capture efficiency is independent of the drive energy between 0.5 and 50 photons. This demonstrates that, although the theoretical capture efficiencies were calculated in the classical limit, they are still valid in the quantum regime. We note that even if the energy calibration is mistuned, the absorption efficiencies quoted in the main text are still valid.

### Check Experiments

We also checked whether the number of averages affects the absorption efficiencies. As the number of averages is increased, the signal amplitude would tend to zero if the signal lacked phase coherence. However, as shown in Fig. S13(a), the signal energy instead is constant once the signal dominates over the noise. Similarly, the absorption efficiencies [Fig. S13(b)] are nearly constant in this regime but are frequently unphysical when the noise is dominant.

The noise energy scales inversely with the number of averages. This makes sense as the energy is proportional to the square of the measured voltage. For large num-



bers of averages, the noise energy becomes constant; we measure the absorption efficiencies near the start of this regime to ensure maximal signal-to-noise ratio. The uncertainties in the absorption efficiency, as calculated with Eq. (S16), are approximately 6% the ratio of the release phase noise energy to the total signal energy.

We also tried to change the coupling  $\kappa$  while keeping  $\kappa T$  and  $\kappa \tau$  constant for pulse length  $T$  and time constant  $\tau$ . When we increased  $\kappa$  to  $1/(18 \text{ ns})$ , the absorption efficiency fell to 98.4% and the receiver efficiency fell to 95.4%. We believe this decrease could be due to not calibrating out the effects of wiring in the fridge, inadequate pulse calibrations, or inadequate sampling resolution of the ADCs.

## ERROR ANALYSIS

Here we explain how to subtract noise to get unbiased estimates of energies. We then calculate the random errors in terms of experimental quantities and consider possible sources of systematic errors.

### Noise Subtraction

We calculate the energies for the absorption efficiency by integrating the magnitude-squared of the signal; however, noise contributes to these calculated energies. Assume that, at the  $k$ th time step, the actual signal is  $(I_k, Q_k)$ , and the noise is  $(x_k, y_k)$  in the  $I$ - and  $Q$ -quadratures, respectively. Then, if the duration of each time step is  $t$  and there are  $N$  time steps, the calculated energy is

$$E_{sig} = t \sum_{k=1}^N [(I_k + x_k)^2 + (Q_k + y_k)^2].$$

The energy in the absence of noise is

$$t \sum_{k=1}^N [I_k^2 + Q_k^2]. \quad (\text{S12})$$

With no signal, the energy is the noise energy

$$E_N = t \sum_{k=1}^N [x_k^2 + y_k^2],$$

so noise energy is measured even without reflections. Hence, the directly measured capture efficiencies are lower than the true values.

To remove this noise contribution, we assume the noise in each quadrature is Gaussian and uncorrelated with noise in the other quadrature, noise at other times, and the signal amplitude. These assumptions are consistent with wide bandwidth white noise in our experiment. We further assume the noise has standard deviation  $\sigma$  and zero mean. With these assumptions, the noise for time step  $k$  can be treated as random values  $g_k$  which are independent with identical Gaussian distributions. Averaging over all such random values gives moments

$$\langle g_k^p \rangle = \frac{1 + (-1)^p}{2} (p-1)!! \sigma^p.$$

Particularly useful moments are  $\langle g_k \rangle = \langle g_k^3 \rangle = 0$ ,  $\langle g_k^2 \rangle = \sigma^2$ , and  $\langle g_k^4 \rangle = 3\sigma^4$ .

Before considering the statistical properties of these energies, we first consider the first and second moments of two useful sums. The first is a weighted sum of Gaussian distributed noise signals given by  $\sum_{k=1}^N w_k g_k$ , where  $w_k$

is the weight of the  $k$ th time step. By the linearity of expectation values,

$$\left\langle \sum_{k=1}^N w_k g_k \right\rangle = 0,$$

while the second moment is

$$\begin{aligned} \left\langle \left( \sum_{k=1}^N w_k g_k \right)^2 \right\rangle &= \sum_{k=1}^N \sum_{l=1}^N w_k w_l \langle g_k g_l \rangle \\ &= \sum_{k=1}^N w_k^2 \langle g_k^2 \rangle + \sum_{k \neq l} w_k w_l \langle g_k \rangle \langle g_l \rangle \\ &= \sigma^2 \sum_{k=1}^N w_k^2, \end{aligned}$$

where we use the Gaussian moments and the independence of noise signals at different times. The other useful sum is a weighted sum of the square of Gaussian distributed noise signals,  $\sum_{k=1}^N w_k g_k^2$  for weights  $w_k$ . By the linearity of expectation values,

$$\left\langle \sum_{k=1}^N w_k g_k^2 \right\rangle = \sigma^2 \sum_{k=1}^N w_k.$$

The second moment of this sum is given by

$$\begin{aligned} \left\langle \left( \sum_{k=1}^N w_k g_k^2 \right)^2 \right\rangle &= \sum_{k=1}^N \sum_{l=1}^N w_k w_l \langle g_k^2 g_l^2 \rangle \\ &= \sum_{k=1}^N w_k^2 \langle g_k^4 \rangle + \sum_{k \neq l} w_k w_l \langle g_k^2 \rangle \langle g_l^2 \rangle \\ &= 3\sigma^4 \sum_{k=1}^N w_k^2 + \sigma^4 \sum_{k \neq l} w_k w_l \\ &= 2\sigma^4 \sum_{k=1}^N w_k^2 + \sigma^4 \left( \sum_{k=1}^N w_k \right)^2. \end{aligned}$$

We can now calculate the mean of  $E_{sig}$  and derive how to subtract the noise contribution. The means of  $E_{sig}$  and  $E_N$  equal

$$\langle E_{sig} \rangle = t \left[ \sum_{k=1}^{N_S} (I_k^2 + Q_k^2) + N_S \sigma_x^2 + N_S \sigma_y^2 \right] \quad (\text{S13})$$

$$\langle E_N \rangle = t [N_N \sigma_x^2 + N_N \sigma_y^2] \quad (\text{S14})$$

where the signal (noise) is measured with  $N_S$  ( $N_N$ ) time steps and the noise in the  $I$  ( $Q$ ) quadrature has standard deviation  $\sigma_x$  ( $\sigma_y$ ). With  $E_N$  rescaled by  $N_S/N_N$ , these means differ by the noiseless energy, so we remove the contribution of noise in a region by:

- Calculate  $E_N$  prior to driving the resonator, so  $I_k = Q_k = 0$ .

- Rescale  $E_N$  by the duration of the desired region.
- Subtract this noise energy from the total measured energy.

This gives an energy

$$E_{sig}^{NS} = E_{sig} - \frac{N_S}{N_N} E_N,$$

which is an unbiased estimate of the noiseless energy [Eq. (S12)].

### Error Analysis

To determine the random uncertainty from this noise, we calculate the variance of both  $E_{sig}$  and  $E_{sig}^{NS}$ . We assume that the following pairs are uncorrelated: noise at different times, noise in the two quadratures, and noise with the signal amplitude. Using the Gaussian moments calculated earlier, we find the following variances:

$$\begin{aligned} \langle (\Delta E_{sig})^2 \rangle &= 4t^2 \sum_{k=1}^{N_S} (I_k^2 \sigma_x^2 + Q_k^2 \sigma_y^2) + 2N_S t^2 (\sigma_x^4 + \sigma_y^4) \\ \langle (\Delta E_N)^2 \rangle &= 2N_N t^2 (\sigma_x^4 + \sigma_y^4). \end{aligned}$$

Since  $E_{sig}$  and  $E_N$  are measured at different times and noise at different times is uncorrelated,  $E_{sig}$  and  $E_N$  are uncorrelated and so the variance in  $E_{NS}$  equals

$$\langle (\Delta E_{sig}^{NS})^2 \rangle = \langle (\Delta E_{sig})^2 \rangle + \left( \frac{N_S}{N_N} \right)^2 \langle (\Delta E_N)^2 \rangle.$$

The additional uncertainty scales as  $\sigma^4$  while the uncertainty in the raw signal energy scales as  $\sigma^2$ . With a large signal-to-noise ratio, the additional noise from this procedure can be neglected.

Further, these variances can be reexpressed in terms of the measured energies  $\langle E_{sig}^{NS} \rangle$  and  $\langle E_N \rangle$  using Eqs. (S13)-(S14). In particular, if  $\sigma_x = \sigma_y$ ,

$$\begin{aligned} \langle (\Delta E_{sig})^2 \rangle &= \frac{2}{N_N} \langle E_{sig}^{NS} \rangle \langle E_N \rangle + \frac{N_S}{N_N^2} \langle E_N \rangle^2 \\ \langle (\Delta E_{sig}^{NS})^2 \rangle &= \frac{2}{N_N} \langle E_{sig}^{NS} \rangle \langle E_N \rangle + \frac{N_S(N_S + N_N)}{N_N^3} \langle E_N \rangle^2 \\ \langle (\Delta E_N)^2 \rangle &= \frac{1}{N_N} \langle E_N \rangle^2. \end{aligned} \quad (\text{S15})$$

We then use these expressions to determine the uncertainty in the absorption efficiency, the ratio of the energy  $E_{abs}^{NS}$  absorbed and then released by the resonator to the total measured energy  $E_{tot}^{NS}$ . However,  $E_{tot}^{NS} = E_{abs}^{NS} + E_{ref}^{NS}$  for reflected energy  $E_{ref}^{NS}$ , so the uncertainties in  $E_{abs}^{NS}$  and  $E_{tot}^{NS}$  are not independent. Similarly, all noise-subtracted energies contain the single term  $\langle E_N \rangle$  and so have correlated uncertainties. Since  $E_{abs}$ ,  $E_{ref}$ , and  $E_N$  are measured at different times, these energies are independent, so their uncertainties can be used to calculate the overall absorption efficiency uncertainty

$$\delta \left( \frac{E_{abs}^{NS}}{E_{tot}^{NS}} \right) = \sqrt{\langle (\Delta E_{abs})^2 \rangle \left( \frac{E_{ref}^{NS}}{(E_{tot}^{NS})^2} \right)^2 + \frac{\langle (\Delta E_{ref})^2 \rangle}{(E_{tot}^{NS})^4} + \langle (\Delta E_N)^2 \rangle \left( \frac{N_{ref} E_{abs}^{NS} - N_{abs} E_{ref}^{NS}}{N_N (E_{tot}^{NS})^2} \right)^2}, \quad (\text{S16})$$

where  $N_{ref}$  and  $N_{abs}$  are the number of data points used to measure  $E_{ref}$  and  $E_{abs}$ , respectively. To verify this uncertainty, we repeated the measurement of the minimal-reflection absorption efficiency 60 times and measured a standard deviation in the absorption efficiency of 0.0552%, within 1% of the 0.0548% expected according to Eq. (S16), validating this error analysis.

The storage efficiency is the ratio of  $E_{abs}^{NS}$  to the total pulse energy  $E_{off}^{NS}$  measured with the coupler off. Since these signals and the noise contributions are measured in different experiments, the uncertainties in these energies are independent, so standard error propagation applies.

These uncertainties only cover random variations but not systematic errors. One major source of systematic errors is poor signal or drive path calibration; this is

a multiplicative effect and so changes the raw energies but not ratios such as the absorption and receiver efficiencies. These efficiencies can, however, be reduced by imperfections in the pulse calibration. We scan over coupler closing delay and drive frequency, measure the resulting absorption efficiencies for an exponentially increasing pulse, and choose parameters which maximize the absorption efficiency. However, this does not include imperfections in the pulse shape, which are likely reducing our measured efficiency as explained in the discussion of the coupler delay in the main text.

- 
- [1] A. N. Korotkov, Phys. Rev. B **84**, 014510 (2011).
- [2] H. Wang *et al.*, Appl. Phys. Lett. **95**, 233508 (2009).
- [3] Y. Yin *et al.*, Phys. Rev. Lett. **110**, 107001 (2013).
- [4] J. M. Martinis, Quantum Inf. Process. **8**, 81 (2009).
- [5] A. Megrant *et al.*, Appl. Phys. Lett. **100**, 113510 (2012).
- [6] J. Wenner *et al.*, Supercond. Sci. Tech. **24**, 065001 (2011).
- [7] Y. Chen *et al.*, Appl. Phys. Lett. **101**, 182601 (2012).
- [8] M. Hofheinz *et al.*, Nature (London) **459**, 546-549 (2009).
- [9] M. Neeley, M. Ansmann, R. C. Bialczak, M. Hofheinz, N. Katz, E. Lucero, A. O'Connell, H. Wang, A. N. Cleland, and J. M. Martinis, Nat. Phys. **4**, 523-526 (2008).
- [10] H. Wang *et al.*, Phys. Rev. Lett. **101**, 240401 (2008).
- [11] M. Hofheinz, E. M. Weig, M. Ansmann, R. C. Bialczak, E. Lucero, M. Neeley, A. D. O'Connell, H. Wang, J. M. Martinis, and A. N. Cleland, Nature (London) **454**, 310-314 (2008).